

# Robust 3D Semantic Occupancy Prediction with Calibration-free Spatial Transformation

Zhuangwei Zhuang\*, Ziyin Wang\*, Sitao Chen\*, Lizhao Liu, Hui Luo, Mingkui Tan<sup>†</sup>

**Abstract**—3D semantic occupancy prediction, which seeks to provide accurate and comprehensive representations of environment scenes, is important to autonomous driving systems. For autonomous cars equipped with multi-camera and LiDAR, it is critical to aggregate multi-sensor information into a unified 3D space for accurate and robust predictions. Recent methods are mainly built on the 2D-to-3D transformation that relies on sensor calibration to project the 2D image information into the 3D space. These methods, however, suffer from two major limitations: First, they rely on accurate sensor calibration and are sensitive to the calibration noise, which limits their application in real complex environments. Second, the spatial transformation layers are computationally expensive and limit their running on an autonomous vehicle. In this work, we attempt to exploit a **Robust and Efficient 3D semantic Occupancy (REO)** prediction scheme. To this end, we propose a calibration-free spatial transformation based on vanilla attention to implicitly model the spatial correspondence. In this way, we robustly project the 2D features to a predefined BEV plane without using sensor calibration as input. Then, we introduce 2D and 3D auxiliary training tasks to enhance the discrimination power of 2D backbones on spatial, semantic, and texture features. Last, we propose a query-based prediction scheme to efficiently generate large-scale fine-grained occupancy predictions. By fusing point clouds that provide complementary spatial information, our REO surpasses the existing methods by a large margin on three benchmarks, including OpenOccupancy, Occ3D-nuScenes, and SemanticKITTI Scene Completion. For instance, our REO achieves **19.8×** speedup compared to Co-Occ, with **1.1%** improvements in geometry IoU on OpenOccupancy. Our code will be available at <https://github.com/ICEORY/REO>.

**Index Terms**—Multi-Sensor Fusion, 3D Semantic Occupancy Prediction, Scene Understanding, Autonomous Driving.

arXiv:2411.12177v1 [cs.CV] 19 Nov 2024

## 1 INTRODUCTION

ACCURATE and comprehensive 3D perception of the surrounding environment is crucial for robotic systems such as autonomous drivings [30], [46] and robotic navigation [5], [22]. To improve the perception ability of autonomous cars, researchers have developed different perception tasks, including object detection [63], [64], semantic segmentation [12], [19], [70], and panoptic segmentation [66], [69] in the 3D space. These tasks, however, fail to provide a comprehensive and coherent representation of the complex outdoor scenes [49]. To address this issue, 3D semantic occupancy prediction, which provides the geometry and semantics of every voxel in the 3D space, has become a fundamental task for modern autonomous systems [13], [16].

As autonomous cars are often equipped with multi-sensor (*i.e.*, multi-cameras and LiDARs), the core of 3D semantic occupancy prediction lies in how to effectively aggregate the features from 2D and 3D sensors in a unified 3D space to generate accurate 3D predictions. The past years have witnessed the great success of BEVFormer-like methods, which represent the multi-view camera features in a bird’s-eye-view (BEV) plane using spatial transformation layers that consist of deformable cross-attention

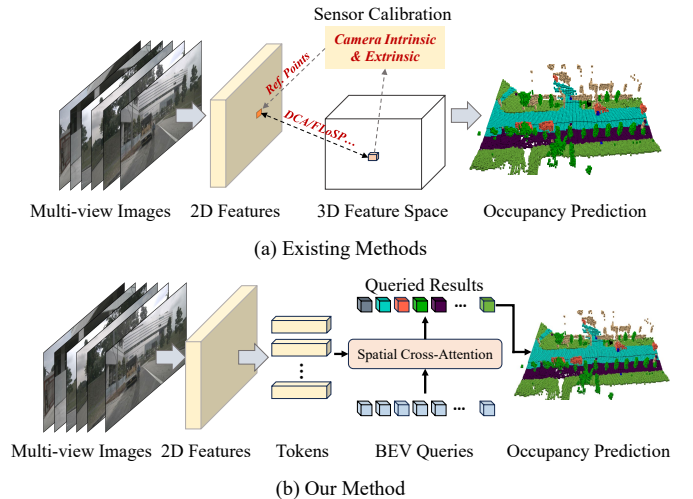


Fig. 1. Comparisons of existing methods [4], [18], [27], [28] and our REO. Unlike existing methods that rely on sensor calibration to compute the reference points of the 3D voxels, our REO directly models the 2D-to-3D spatial correspondence by attention scheme without using sensor calibration. We simplify the architecture diagram for better illustration.

- Zhuangwei Zhuang, Sitao Chen, Lizhao Liu and Mingkui Tan are with the School of Software Engineering, South China University of Technology. Zhuangwei Zhuang is also with Robosense Inc., ShenZhen, China. Mingkui Tan is also with the Puzhou Laboratory, Guangzhou, China. E-mail: {z.zhuangwei, mechenst, selizhaoliu}@mail.scut.edu.cn, mingkuitan@scut.edu.cn.
- Ziyin Wang is with Robosense Inc., ShenZhen, China. E-mail: wang2457@purdue.edu.
- Hui Luo is with the National Key Laboratory of Optical Field Manipulation Science and Technology, CAS, also with the Institute of Optics and Electronics, CAS, Chengdu, China. E-mail: luohui19@mailsucas.ac.cn.
- \*Authors contribute equally. <sup>†</sup> Corresponding author.

(DCA) and deformable self-attention (DSA) layers [28], [50], [59]. Recent studies further improve the representation ability of deep models by aggregating the image features in a tri-perspective (TPV) plane [18]. Despite their effectiveness, these methods, however, require calibration information (*i.e.*, intrinsic or extrinsic of the sensors) to aggregate the features around the reference points from

TABLE 1

Inference time of spatial transformation in existing methods. Both VoxFormer and TPVFormer use DSA+DCA to lift the image feature. MonoScene uses FLoSP to project the image features into 3D space. We report the results evaluated on SemanticKitti Scene Completion.

Methods	Spatial Transform.	Total	Percentage (%)
VoxFormer [27]	72.75ms	80.45ms	90.42%
TPVFormer [18]	118.99ms	172.96ms	68.80%
MonoScene [4]	78.81ms	145.26ms	54.25%
REO (Ours)	5.02ms	44.26ms	11.34%

multi-view cameras(as shown in Figure 1(a)). The coordinates of reference points may be inaccurate due to the calibration noise in real-life applications and may degrade the model performance of these methods [21], [33]<sup>1</sup>. Moreover, limited by the 2D-to-3D projection scheme, these methods often obtain sparse features and require multi-resolution BEV/TPV queries to generate fine-grained occupancy predictions<sup>2</sup>. As a result, the computational costs of these methods are unaffordable for real-life applications [60] (See Table 1).

In this work, we argue that the dependency on sensor calibration information can be eliminated, motivated by the fact that *Humans can learn to reconstruct the physical world in the brain even without knowing the exact positions of eyes (a.k.a. sensor extrinsic parameters)*. Moreover, inspired by [67], which implicitly learns a mapping from multi-cameras into a 2D map-view representation using a cross-view attention mechanism, we further explore a Calibration-free Spatial Transformation paradigm that implicitly learns the 2D-to-3D spatial representation with vanilla cross-attention scheme. Specifically, as shown in Figure 1(b), given sampled voxels in the 3D space, we obtain the occupancy predictions directly from multi-view images via cross-attention modules. As the cross-attention scheme considers the full correlation between 2D features and 3D space, it is insensitive to the sensor calibration noise. Though the idea is straightforward, it suffers from two limitations. **First**, the computational costs and memory requirements are unaffordable due to the high-resolution nature of multi-view images and a vast number of queried voxels ( $\sim 10^5$  on Occ3D-nuScenes). **Second**, it is difficult to dig out both the spatial correspondence and discriminative features from multi-view images without spatial prior from sensor calibration information [6].

To address these issues, we exploit a Robust and Efficient Occupancy (REO) prediction scheme with calibration-free spatial transformation based on vanilla cross-attention. Specifically, we first extract the image features by a pre-trained 2D encoder and propose an image feature aggregation module to aggregate the features from different cameras. Then, we propose calibration-free spatial-transformation modules based on cross-attention to transform the image features into a compact BEV plane. Third, we lift the BEV features to voxel space and introduce a query-based prediction scheme to generate both geometry and semantic predictions efficiently. As it is difficult to learn both 2D-to-3D projection and semantic representations without spatial prior, we introduce auxiliary 2D and 3D training tasks to enhance the discrimination power of the image backbone on spatial, textural, and semantic features. The main contributions of this work are summarized as follows.

- We find that the sensor calibration for multi-sensor fusion can

1. See discussions in Sec. 4.5.  
2. See discussions in Sec. 5.5.

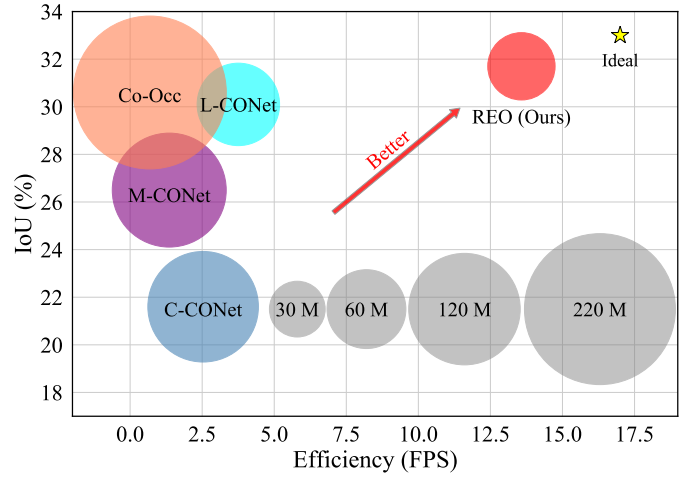


Fig. 2. Comparisons of model efficiency and performance of different methods on OpenOccupancy.

be discarded during inference by introducing calibration-free spatial transformation (CST) modules based on the vanilla attention scheme. With the proposed CST, our REO is robust in calibration noise of sensor-calibration information (*i.e.*, camera intrinsic and extrinsic parameters).

- We introduce both 2D and 3D auxiliary training tasks, including depth regression, semantic segmentation, and texture reconstruction, to enhance the discrimination power of the image backbone and effectively improve the performance of the occupancy model.
- We propose a query-based prediction scheme to efficiently predict the geometry and semantic occupancy results of sampled queried voxels in 3D space. Moreover, compared to the state-of-the-art fusion-based method (*i.e.*, Co-Occ), our REO achieves **19.8** $\times$  acceleration with **1.1**% improvements in geometry IoU on OpenOccupancy.

## 2 RELATED WORK

**Multi-sensor fusion based perception** As cameras and LiDAR can provide complementary information, many works [10], [38], [52], [70] aim to efficiently fuse the multi-sensor features for accurate and robust 3D perception. RGBAL [10] converts RGB images to a polar-grid mapping representation and designs early and mid-level fusion architectures. EPMF [47], [70] projects the point clouds to the camera coordinate system using perspective projection and proposes a collaborative fusion scheme with perception-aware loss. 2DPASS [62] designs a multi-scale fusion-to-single knowledge distillation strategy to distill multi-modal knowledge to single point cloud modality. M-CONet [55] constructs a LiDAR branch and a camera branch for point clouds and images, respectively, and projects queries to sample from 2D image features and 3D voxel features and fuses them through an adaptive fusion module. Recent works(*e.g.*, DeepFusion [26], FUTR3D [8], UniSeg [32]) attempt to mitigate the problem of feature misalignment by a learnable sensor fusion. Different from the existing fusion-based method, our REO is camera-centric and only uses a small number of voxelized point clouds, reducing the dependency on expensive high-resolution LiDAR. Besides, the multi-modality features are implicitly aligned

via cross-attention modules without leveraging spatial prior from calibration information.

**2D-to-3D spatial transformation** Vision-based perception has recently gained much attention due to its cost-effectiveness and rich appearance information. A crucial step in these methods is to project 2D image features into 3D space. One paradigm follows the forward projection. Lift-Splat-Shoot [41] performs 2D-to-3D projection based on the estimated pixel-wise depth distribution. BEVDepth [25] leverages depth supervision derived from point clouds to guide depth learning. BEVStereo [24] further proposes a dynamic temporal stereo technique to enhance depth estimation. MatrixVT [68] introduces Prime Extraction and the Ring & Ray Decomposition to accelerate the feature transformation. Another paradigm follows the backward projection. OFT [42] and ImVoxelNet [44] reconstruct 2D image features to 3D voxels along the camera rays with the corresponding intrinsic and extrinsic camera parameters. DETR3D [57] projects the predefined learnable 3D queries onto 2D images to sample the corresponding features. BEVFormer [28] designs deformable cross-attention to aggregate the spatial features from multi-camera images and generate BEV features. FB-BEV [29] leverages the two paradigms and performs the forward-backward projection to transform the multi-view image features into BEV representation. In addition, PETR [33] proposes to encode 3D coordinate information into 2D image features to generate 3D position-aware features. Note that existing works still require calibration information of cameras to perform 2D-to-3D projection, thus inevitably affected by the calibration noise. In contrast, Zhou *et al.* [67] implicitly model the spatial correspondence between multi-camera and map-view representation for 2D map-view semantic segmentation. We further exploit such an idea on complex multi-modal 3D semantic occupancy prediction.

**3D semantic occupancy prediction** Recently, researchers have investigated 3D semantic occupancy prediction that provides a comprehensive and coherent perception of the outdoor environment [18], [28], [71]. BEVFormer [28] first defines learnable grid-shaped BEV (bird’s-eye-view) queries that capture spatial information from multi-view images with deformable attention layers. TPVFormer [18] further designs a tri-perspective view (TPV) representation that accompanies BEV with two additional perpendicular planes to describe a stereoscopic 3D scene. SurroundOcc [59] defines voxel queries rather than BEV queries to fuse multi-camera information with 2D-to-3D spatial attention and applies 3D convolution to construct 3D volume features in a multi-scale fashion. VoxFormer [27] adopts a two-stage design where a query proposal network picks out reliable voxel queries and a sparse-to-dense MAE-like architecture generates dense semantic voxels. However, these methods rely on accurate sensor calibration information to compute the reference points for multi-view image feature aggregation. The model performance may degrade due to the calibration noise in real application scenarios. Unlike these works, our method directly aggregates the multi-view image features by vanilla cross-attention layers, discarding the reference points. To the best of our knowledge, our REO is the first work to exploit calibration-free multi-sensor feature fusion for 3D semantic occupancy prediction.

### 3 PROPOSED METHOD

As illustrated in Figure 3, our REO consists of a feature aggregation module (Section 3.2), calibration-free spatial transformation for both cameras and LiDAR (Section 3.3), and query-based prediction

---

#### Algorithm 1 General Scheme of REO

---

**Input:** Training data  $\{\mathcal{I}, \mathbf{P}, \mathbf{O}\}$ , sampled queries  $\mathbf{V}^{fine}$ , hyperparameter  $\lambda_{focal}, \lambda_{dice}, \lambda_{rgb}, \lambda_{depth}$  and model  $M$ .

- 1: **while** *not converged* **do**
  - 2:   Sample an image  $\mathbf{I}_n$  from multi-view images  $\mathcal{I}$  and obtain the 2D predictions.
  - 3:   Compute the objectives of 2D auxiliary tasks according to Eqs.(13) and (14).
  - 4:   Compute the voxelized point clouds features  $\mathbf{V}^{LiDAR}$  and obtain the LiDAR feature token  $\mathbf{T}^{LiDAR}$  using Eq.(5).
  - 5:   Project the LiDAR feature to BEV plane by the proposed REO module and obtain  $\mathbf{B}^{LiDAR}$ .
  - 6:   Aggregate the image features from pre-trained image backbones and obtain the image tokens  $\mathbf{T}_n^{cam}$  w.r.t. the multi-view images.
  - 7:   Use BEV features w.r.t. LiDAR as queries and project the multi-view image features to BEV plane by REO module.
  - 8:   Lift the BEV features to voxel space and compute coarse predictions by Eqs.(8) and (9).
  - 9:   Compute the fine-grained predictions by grid sample and compute the 3D predictions by Eqs.(10) and (11).
  - 10:   Compute the objectives w.r.t. the 2D/3D tasks and optimize model  $M$  by minimizing the objective in Eq.(17).
  - 11: **end while**
- 

scheme (Section 3.4). Different from existing methods [4], [18] that only use 3D semantic occupancy labels for supervision, we exploit 2D and 3D auxiliary training tasks including depth regression, semantic segmentation, and texture reconstruction (Section 3.5) to help the image backbone capture spatial and semantic features. The overall training scheme of our method is shown in Algorithm 1.

#### 3.1 Problem definition

Let  $\mathcal{I} = \{\mathbf{I}_1, \mathbf{I}_2, \dots, \mathbf{I}_N\}$  be the input multi-view images, where  $\mathbf{I}_n \in \mathbb{R}^{3 \times H_{in} \times W_{in}}$  denotes the RGB image w.r.t. the  $n$ -th camera.  $H_{in}, W_{in}$  denote the height, and width of the image. Let  $\mathbf{P} \in \mathbb{R}^{N_{point} \times 4}$  be a point cloud from LiDAR with  $N_{point}$  points. The target of 3D semantic occupancy prediction is to predict the semantic class of each voxel in the  $\mathbf{O} \in \mathbb{R}^{H \times W \times D}$  voxel space using multi-sensor information (*e.g.*, cameras and LiDAR) and indicate whether the voxel is empty or belongs to a specific semantic class  $s \in \{0, 1, 2, 3, \dots, S\}$ . Here,  $S$  is the number of semantic classes, and 0 often denotes the free voxel.  $H, W, D$  denote the height, width, and length of the 3D voxel space, respectively.

Note that it is unnecessary to obtain the full prediction results of 3D space in practice, one can only compute the occupancy results w.r.t. voxels in the interested region. Specifically, given voxels in 3D interested region, the occupancy prediction is computed by

$$\hat{\mathbf{O}} = M(\mathbf{V}, \mathcal{I}, \mathbf{P}), \quad (1)$$

where  $\mathbf{V} \in \mathbb{R}^{Q \times 3}$  denotes the voxels with position  $(h, w, d)$  in the 3D space.  $Q = H \times W \times D$  indicates the number of voxels.  $M(\cdot)$  denotes the deep model.

#### 3.2 Image feature aggregation

Following [18], we adopt a pre-trained image encoder (*e.g.*, ResNet-50 [15]) to extract 2D image features. Different from existing methods [28], we do not use a feature pyramid network (FPN) to



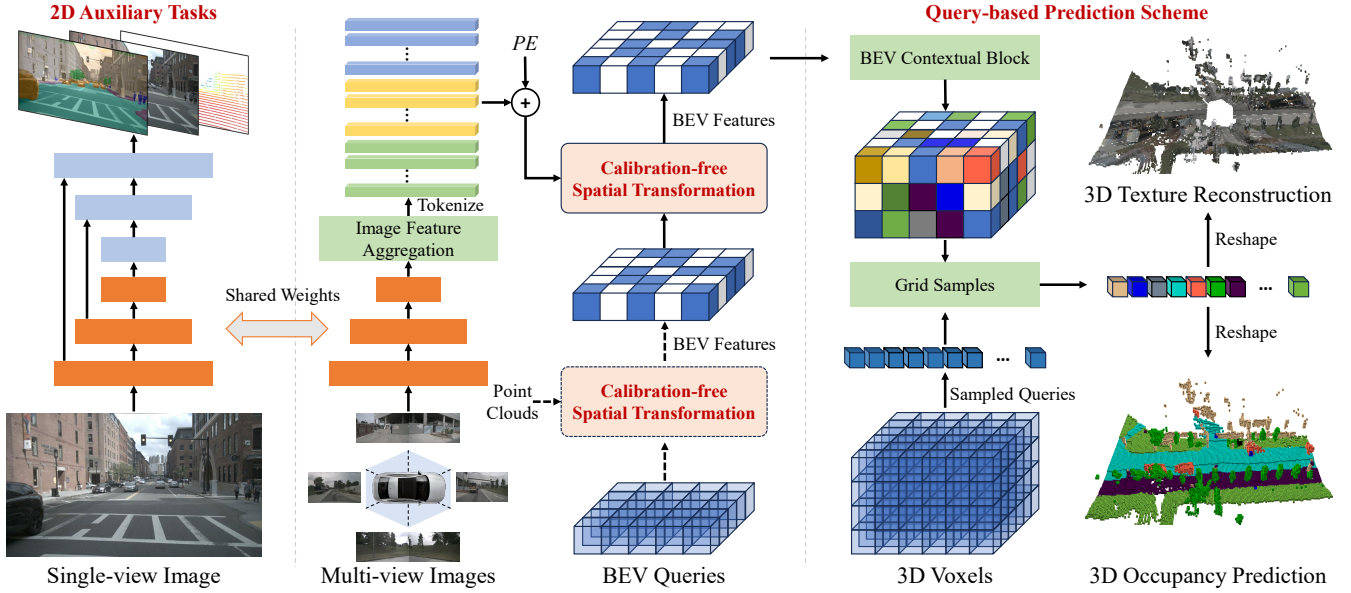


Fig. 3. Overview of the proposed Robust and Efficient Occupancy (REO) Prediction. We first extract image features from multi-cameras using a pre-trained 2D encoder. Then, we aggregate the image features with a feature aggregation module. Both multi-cameras and LiDAR features are efficiently transformed to the BEV plane by the calibration-free spatial transformation modules. Third, we introduce 2D/3D auxiliary training tasks to ease the spatial projection and improve the model performance. Last, we use a query-based prediction scheme to efficiently generate predictions of queried voxels sampled from 3D space.

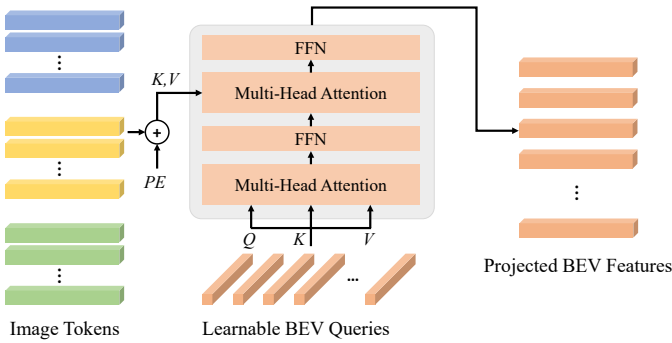


Fig. 4. Illustration of calibration-free spatial transformation for multi-cameras.  $PE$  indicates the positional embeddings. The features from multi-view images are projected to a predefined BEV plane with the vanilla attention scheme. For multi-sensor fusion, the learnable BEV queries are replaced by the projected BEV LiDAR features.

aggregate the multi-level image features by considering the model efficiency. Instead, we use the features  $\mathbf{H}_n^l$  from the  $l$ -layer of the image backbone.  $\mathbf{H}_n \in \mathbb{R}^{C_l \times H_l \times W_l}$  indicate the features w.r.t. the  $l$ -layer and  $n$ -camera. Then, we apply the spatial attention module (SAM) [2] to augment the features and use a self-attention layer to learn the inner correspondence of features w.r.t. each camera.

### 3.3 Calibration-free spatial transformation

**Spatial transformation for multi-cameras.** To lift the 2D image features to 3D space, a common practice is to use deformable cross-attention (DCA) [18], [28] with reference points determined by the calibration information (*i.e.*, camera extrinsic and intrinsic). As a result, the model performance is degraded when introducing noise to the sensor calibration. To address this issue, we proposed a calibration-free spatial transformation that built upon vanilla

cross-attention layers to obtain 3D features without using sensor calibration (See Figure 4).

Let  $\mathbf{F}_n^{cam} \in \mathbb{R}^{C_f \times H_f \times W_f}$  be the merged image features w.r.t. the  $n$ -th camera.  $C_f$  indicates the number of channels of the image features.  $H_f$  and  $W_f$  denote the height and width of the features, respectively. Then, the image features are converted to a set of tokens by flattening the spatial dimensions. The feature tokens  $\mathbf{T}_n^{cam} \in \mathbb{R}^{N_t \times C_t}$  w.r.t. the  $n$ -th image features are computed by

$$\mathbf{T}_n^{cam} = \text{Tokenizer}(\mathbf{F}_n^{cam}), \quad (2)$$

where  $N_t$  and  $C_t$  indicate the length and embedding dimensions of the feature tokens, respectively.

Similar to BevFormer [28], we adopt learnable embedding  $\mathbf{Q} \in \mathbb{R}^{N_{bev} \times C_t}$  as queries to aggregate the feature tokens from multi-cameras to a predefined compact BEV plane.  $N_{bev} = H_{bev} \times W_{bev}$  denotes the length of BEV queries. Given points  $\mathbf{P} \in \mathbb{R}^{N_{bev} \times 2}$  from the BEV plane, we compute the BEV queries  $\mathbf{Q}$  by

$$\mathbf{Q} = \text{PositionEncoding}(\mathbf{P}) + \mathbf{W}, \quad (3)$$

where  $\mathbf{W} \in \mathbb{R}^{N_{bev} \times C_t}$  denotes the learnable positional embedding.  $\text{PositionEncoding}(\cdot)$  indicate positional encoding layer [51].

With the vanilla cross-attention scheme, the projected image BEV feature  $\mathbf{B}^{cam} \in \mathbb{R}^{N_{bev} \times C_t}$  is computed by

$$\mathbf{B}^{cam} = \text{SpatialCrossAttn}(\mathbf{Q}, \mathbf{T}). \quad (4)$$

**Spatial transformation for LiDAR** With the proposed calibration-free spatial transformation, we can obtain the BEV representations from multi-view 2D images. As point clouds provide complementary spatial information of images, one can further fuse the LiDAR features to improve the model performance. However, since the high-resolution LiDAR is expensive, we only consider fusing a small number of voxelized point clouds with lower resolution to reduce the dependency on LiDAR.<sup>3</sup>

3. See experiments in Table 6.



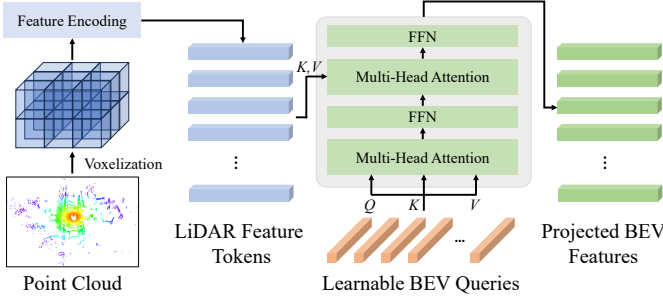


Fig. 5. Illustration of calibration-free spatial transformation for LiDAR. We assume that the LiDAR coordinate differs from the ground truth coordinate. Therefore, we use REO to project the LiDAR features to the predefined BEV plane with an attention scheme.

Given a point cloud from LiDAR with  $N_{point}$  points. Each point in the point cloud contains a 3D coordinate  $(x, y, z)$  and an intensity value  $(i)$ . As shown in Figure 5, we voxelize the point clouds and randomly sample  $N_{LiDAR}$  voxels. Each LiDAR voxel contains the coordinates  $\{x, y, z, i\}$  of the point, where  $i$  indicates the intensity value. We also compute the density and range value  $r = \sqrt{x^2 + y^2 + z^2}$  of each voxel. Then, we use a position encoding layer [51] to convert the voxels into feature tokens. The LiDAR feature tokens  $\mathbf{T}^{LiDAR} \in \mathbb{R}^{N_{LiDAR} \times C_t}$  is computed by

$$\mathbf{T}^{LiDAR} = \text{PositionEncoding}(\mathbf{V}^{LiDAR}), \quad (5)$$

where  $N_{LiDAR}$  indicates the length of LiDAR tokens.  $\mathbf{V}^{LiDAR} \in \mathbb{R}^{N_{LiDAR} \times 6}$  denotes a set of LiDAR voxels.

Note that we cannot compute the BEV representation of point clouds and fuse the image features by concatenation directly when the extrinsic of LiDAR is missing. Besides, the LiDAR coordinates may also differ from the ground truth coordinates. Similar to the CFL module of cameras, we also use vanilla attention modules to align the point cloud features to ground truth coordinates and conduct feature fusion with cameras. Specifically, for LiDAR-only implementation, we compute the BEV representation of LiDAR  $\mathbf{B}^{LiDAR} \in \mathbb{R}^{N_{bev} \times C_t}$  by

$$\mathbf{B}^{LiDAR} = \text{SpatialCrossAttn}(\mathbf{Q}, \mathbf{T}^{LiDAR}). \quad (6)$$

To multi-modal fusion, we use  $\mathbf{B}^{LiDAR}$  as BEV queries to lift the image feature to the BEV plane. Thus, similar to Eq.(4), the fused BEV features are computed by

$$\mathbf{B}^{fuse} = \text{SpatialCrossAttn}(\mathbf{B}^{LiDAR}, \mathcal{T}). \quad (7)$$

### 3.4 Query-based prediction scheme

Due to the huge number of predicted voxels (e.g.,  $10^5$  voxels on Occ3D-nuScenes and  $10^7$  voxels on OpenOccupancy), it would be computationally expensive to predict fine-grain occupancy prediction directly. Besides, it is unnecessary to predict all voxels with fine grid size as the 3D space is extremely sparse. Therefore, we first introduce BEV context blocks to enhance the contextual feature of BEV representation and lift the BEV features to voxel representations by reshaping the feature channels. Then, we use the MLP layer to generate coarse predictions with low resolutions from the voxelized features. Last, we compute the fine-grained prediction of queried voxels from low-resolution coarse predictions by grid sample.

Let  $\mathbf{B} \in \mathbb{R}^{C_t \times H_{bev} \times W_{bev}}$  be the BEV feature reshaped from the outputs of spatial cross-attention. To enhance the contextual features of BEV representations, we adopt contextual blocks introduced in [9]. The enhance BEV feature  $\mathbf{B}^{context}$  is computed by

$$\mathbf{B}^{context} = \text{ContextualBlock}(\mathbf{B}). \quad (8)$$

where  $\mathbf{B}^{context} \in \mathbb{R}^{C_{context} \times H_{bev} \times W_{bev}}$ . Then, we split the channels of  $\mathbf{B}^{context}$  to obtain voxel representation  $\mathbf{V}^{coarse} \in \mathbb{R}^{C_{coarse} \times H_{bev} \times W_{bev} \times D_{coarse}}$ . Here,  $C_{context} = C_{coarse} \times D_{coarse}$  denotes the number of channels w.r.t. BEV features.  $C_{coarse}$  denotes the channels of voxel features.

Then, we adopt the MLP layer to obtain occupancy predictions. The coarse semantic prediction  $\hat{\mathbf{O}}_{sem}^{coarse} \in \mathbb{R}^{(S+1) \times H_{coarse} \times W_{coarse} \times D_{coarse}}$  is computed by

$$\hat{\mathbf{O}}_{sem}^{coarse} = \text{MLP}(\mathbf{V}^{coarse}). \quad (9)$$

Alternatively, we also obtain the geometry prediction  $\hat{\mathbf{O}}_{geo}^{coarse} \in \mathbb{R}^{2 \times H_{coarse} \times W_{coarse} \times D_{coarse}}$  from the semantic predictions.

Given  $\mathbf{V}^{fine} \in \mathbb{R}^{N_{fine} \times 3}$  sampled from the fine-grained voxel space, we further interpolate the fine predictions with a grid sample. Specifically, the geometry and semantic fine-grained predictions are computed by

$$\begin{cases} \hat{\mathbf{O}}_{sem}^{fine} = \text{GridSample}(\hat{\mathbf{O}}_{sem}^{coarse}, \mathbf{V}^{fine}), \\ \hat{\mathbf{O}}_{geo}^{fine} = \text{GridSample}(\hat{\mathbf{O}}_{geo}^{coarse}, \mathbf{V}^{fine}). \end{cases} \quad (10)$$

### 3.5 Construction of 2D/3D auxiliary training tasks

In semantic occupancy prediction, it is challenging to learn both the 2D-to-3D projection and semantics from multi-view images without spatial prior. In this section, we first propose a 3D texture reconstruction task to ease the learning of 2D-to-3D projection. Then, we introduce the 2D auxiliary training tasks to enhance both the semantic and spatial features of the 2D image backbone.

**3D texture reconstruction** Motivated by the scheme of auto-encoder [14], we model the learning of spatial correspondence by 2D-to-3D texture reconstruction. Similar to Eqs.(9) and (10), we predict the texture of voxels by

$$\hat{\mathbf{O}}_{rgb} = \text{GridSample}(\text{MLP}(\mathbf{V}^{coarse}), \mathbf{V}^{fine}), \quad (11)$$

where  $\hat{\mathbf{O}}_{rgb} \in \mathbb{R}^{N_{fine} \times 3}$  indicates the predicted RGB color w.r.t. the voxels  $\mathbf{V}^{fine}$ . Let  $\mathbf{O}_{rgb}$  be the ground truth color of the queried voxel (i.e., 3D texture cues). The auxiliary loss of the 3D texture reconstruction task is defined as

$$\mathcal{L}_{rgb}^{3D} = \text{SmoothL1}(\hat{\mathbf{O}}_{rgb}, \mathbf{O}_{rgb}). \quad (12)$$

Note that the 3D texture cues are from the observations of the physical world and can be obtained by scene reconstruction [36]. For convenience, we project the image to 3D voxels to construct the 3D texture cues in this work.

**2D auxiliary training tasks.** By considering the model efficiency, we do not adopt a heavy 3D decoder that is computationally expensive for occupancy predictions. However, it may also result in unsatisfied model performance. To address this issue, we propose three 2D auxiliary tasks to enhance the discrimination power of 2D backbone, including semantic segmentation, depth regression, and texture reconstruction.

Given  $\mathbf{I}_n \in \mathbb{R}^{3 \times H_{in} \times W_{in}}$  sampled from multi-view images  $\mathcal{I}$ , we adopt a FPN to fuse the multi-level features  $\mathcal{H}_n = \{\mathbf{H}_n^l\}_{l=1}^L$  from the image backbone obtain the 2D predictions. For the

TABLE 2  
Comparisons of three benchmark data sets.

Data set	OpenOccupancy	Occ3D-nuScenes	SemanticKITTI
Grid size	0.2m	0.4m	0.2m
#Point Clouds	34720	34720	122820
#Voxelized Point Clouds	11088	6811	27140
Compression Rate	31.9%	19.6%	22.1%

semantic segmentation task, we use multi-class focal loss and dice loss as objectives. Thus, the objectives w.r.t. the semantic segmentation task are formulated as

$$\begin{aligned} \mathcal{L}_{sem}^{2D} = & \lambda_{focal} \mathcal{L}_{focal}(\hat{\mathbf{Y}}_{sem}, \mathbf{Y}_{sem}) \\ & + \lambda_{dice} \mathcal{L}_{dice}(\hat{\mathbf{Y}}_{sem}, \mathbf{Y}_{sem}), \end{aligned} \quad (13)$$

where  $\hat{\mathbf{Y}}_{sem} \in \mathbb{R}^{S \times H_{in} \times W_{in}}$  and  $\mathbf{Y}_{sem} \in \mathbb{R}^{S \times H_{in} \times W_{in}}$  denote the predictions and ground truth of 2D semantic segmentation.  $\lambda_{focal}$  and  $\lambda_{dice}$  are the hyper parameters to balance the two terms. Following [70], we project the LiDAR semantic labels to the image to obtain the 2D semantic labels.

For both the depth regression and texture reconstruction tasks, we use the smooth L1 loss as the objective. Therefore, the object functions are formulated as

$$\begin{cases} \mathcal{L}_{depth}^{2D} = \lambda_{depth} \text{SmoothL1}(\hat{\mathbf{Y}}_{depth}, \mathbf{Y}_{depth}), \\ \mathcal{L}_{rgb}^{2D} = \lambda_{rgb} \text{SmoothL1}(\hat{\mathbf{Y}}_{rgb}, \mathbf{Y}_{rgb}). \end{cases} \quad (14)$$

where  $\hat{\mathbf{Y}}_{depth}$  and  $\mathbf{Y}_{depth}$  denote the predictions and labels of depth regression, respectively.  $\hat{\mathbf{Y}}_{rgb}$  and  $\mathbf{Y}_{rgb}$  denote the predictions and labels of texture reconstruction, respectively.  $\lambda_{depth}$  and  $\lambda_{rgb}$  are the hyper parameters to balance the objectives.  $\mathbf{Y}_{depth}$  is obtained by projecting the point clouds to 2D images. The decoder w.r.t. 2D auxiliary training is dropped to reduce model complexity during inference.

### 3.6 Formulation of objective

To optimize the occupancy network, we use focal loss [31] and dice loss [45] as objectives. The objective of semantic occupancy prediction is defined as

$$\begin{aligned} \mathcal{L}_{sem}^{3D} = & \lambda_{focal} \mathcal{L}_{wce}(\hat{\mathbf{O}}_{sem}^{fine}, \mathbf{O}_{sem}^{fine}) \\ & + \lambda_{dice} \mathcal{L}_{dice}(\hat{\mathbf{O}}_{sem}^{fine}, \mathbf{O}_{sem}^{fine}). \end{aligned} \quad (15)$$

Similar to the semantic occupancy predictions, the objective of geometry predictions is defined as

$$\begin{aligned} \mathcal{L}_{geo}^{3D} = & \lambda_{focal} \mathcal{L}_{wce}(\hat{\mathbf{O}}_{geo}^{fine}, \mathbf{O}_{geo}^{fine}) \\ & + \lambda_{dice} \mathcal{L}_{dice}(\hat{\mathbf{O}}_{geo}^{fine}, \mathbf{O}_{geo}^{fine}). \end{aligned} \quad (16)$$

Considering the objective of all the above tasks, we formulate the object function of our proposed REO as

$$\mathcal{L} = \mathcal{L}_{geo}^{3D} + \mathcal{L}_{sem}^{3D} + \mathcal{L}_{rgb}^{3D} + \mathcal{L}_{sem}^{2D} + \mathcal{L}_{depth}^{2D} + \mathcal{L}_{rgb}^{2D}. \quad (17)$$

## 4 EXPERIMENTS

### 4.1 Data sets and evaluation metrics

**Data sets** Following [18], [49], [55], we evaluate our method on OpenOccupancy [55], Occ3D-nuScenes [49], and SemanticKITTI Scene Completion [1].

**OpenOccupancy** is an occupancy prediction data set based on nuScenes, which provides 360-degree point clouds and images. The dataset has a scene range from  $[-51.2m, -51.2m, -5m]$  to  $[51.2m,$

$51.2m, 3m]$ . The 3D space is voxelized to  $512 \times 512 \times 40$  with a grid size of  $0.2m$ . It contains 700 scenes for training and 150 scenes for validation, respectively. Besides, it has 16 classes for semantic occupancy prediction. **Occ3D-nuScenes** is a 3D semantic occupancy prediction dataset based on nuScenes [3], but with a scene range from  $[-40m, -40m, -1m]$  to  $[40m, 40m, 5.4m]$  along X, Y, and Z axes, which is voxelized into  $200 \times 200 \times 16$  given a voxel size of  $0.4m$ . Note that Occ3D-nuScenes has 16 semantic classes and an additional unknown object class. Therefore, it has 17 semantic classes. **SemanticKITTI** is a large-scale outdoor data set based on the KITTI Odometry Benchmark [11], which provides 360-degree point clouds and front-view images. For the semantic scene completion task [1], the dataset has a valid evaluation range from  $[0m, -25.6m, -2m]$  to  $[51.2m, 25.6m, 4.4m]$  along X, Y, and Z axes, which is voxelized into  $256 \times 256 \times 32$ . Each voxel has a size of  $0.2m \times 0.2m \times 0.2m$  and is assigned a label from 21 classes (19 semantics, 1 empty, 1 unknown). SemanticKITTI divides its 22 sequences into three sets: sequences 00-10 except 08 for training, sequence 08 for validation, and sequences 11-21 for testing, respectively.

**Evaluation Metrics** Following [4], [18], we use the intersection over union of scene completion (SC IoU) that ignores the semantic labels to evaluate the quality of scene completion on SemanticKITTI. Besides, we also report the semantic scene completion mean IoU (SSC mIoU) of all semantic classes on SemanticKITTI. For Occ3D-nuScenes, we report the mean IoU (mIoU) of 16 semantic classes [49]. For OpenOccupancy, we follow the common practice of [55] and report both the mean IoU(mIoU) of 17 semantic classes and the IoU of geometry occupancy prediction.

### 4.2 Implementation details

We implement our method using PyTorch [40] and use ResNet-50 [15] as the backbone of the 2D image encoder. The parameters of the image encoder are initialized by ImageNet pre-trained weights from [40]. The length of embeddings  $C_t$  is set to 384 empirically. We train the networks using AdamW [35] for 25 epochs on all the benchmark data sets. The learning rate starts at 0.0004 and decays to 0 with a cosine policy [34]. The weight decay is 0.01. The batch size is 16 for nuScenes and 8 for SemanticKITTI, respectively. The grid sizes of BEV queries are set to  $1.6m$  and  $0.8m$  on nuScenes and SemanticKITTI, respectively. On all the data sets,  $\lambda_{focal}$ ,  $\lambda_{dice}$  and  $\lambda_{rgb}$  are set to 1.0, and  $\lambda_{depth}$  is set to 2.0. The input images are resized to  $448 \times 800$  on nuScenes and  $358 \times 1184$  on SemanticKITTI, respectively. As shown in Table 2, we count the average number of points and voxels of the point clouds on three data sets. Therefore, we set the number of sampled voxelized point clouds to 10240, 5120, and 20480 on OpenOccupancy, Occ3D-nuScenes, and SemanticKITTI, respectively.

### 4.3 Comparisons on benchmark data sets

**Results on OpenOccupancy.** To compare our method with the state-of-the-art methods (e.g., M-CONet [55], M-OccGen [53], and Co-Occ [39]), we evaluate our method on OpenOccupancy [55]. As shown in Table 3, we report both the semantic metric mIoU and geometry metric IoU on OpenOccupancy. From the results, our REO outperforms existing fusion-based methods in geometry IoU and achieves comparable performance in semantic mIoU. Note that existing LiDAR-only and fusion-based methods often stack multi-sweep point clouds as inputs. For a fair comparison, we

TABLE 3

Comparisons on OpenOccupancy validation set. Cons. Veh represents construction vehicle and Dri. Sur denotes driveable surface, respectively. The **bold** numbers indicate the best results. † indicates the results with multi-sweep point clouds.

Method	Modality	IoU (%)	mIoU (%)	barrier	bicycle	bus	car	Cons. Veh	motorcycle	pedestrian	traffic cone	trailer	truck	Dri. Sur	other flat	sidewalk	terrain	manmade	vegetation
MonoScene [4]	C	17.1	7.2	7.3	4.3	9.6	7.1	6.2	3.5	5.9	4.7	5.6	4.9	15.6	6.8	7.9	7.6	10.5	7.9
TPVFormer [18]	C	15.1	8.3	9.7	4.5	11.5	10.7	5.5	4.6	6.3	5.4	6.9	6.9	14.1	9.8	8.9	9.0	9.9	8.5
LMSCNet† [43]	L	26.7	11.8	12.9	5.2	12.8	12.6	6.6	4.9	6.3	6.5	8.8	7.7	24.3	12.7	16.5	14.5	14.2	22.1
JS3C-Net† [61]	L	29.6	12.7	14.5	4.4	13.5	12.0	7.8	4.4	7.3	6.9	9.2	9.2	27.4	15.8	15.9	16.4	14.0	24.8
SparseOcc [48]	C	21.8	14.1	16.1	9.3	15.1	18.6	7.3	9.4	11.2	9.4	7.2	13.0	31.8	21.7	20.7	18.8	6.1	10.6
L-COCCNet [55]	C	21.6	13.6	13.6	8.4	14.7	18.3	7.1	11.0	11.8	8.8	5.2	13.0	32.7	21.1	20.1	17.6	5.1	8.4
L-COCCNet† [55]	L	30.1	15.9	18.0	3.9	14.2	18.7	8.3	6.3	11.0	5.8	14.1	14.3	35.3	20.2	21.5	20.9	19.2	23.0
M-COCCNet† [55]	C&L	26.5	20.5	23.3	16.1	22.2	24.6	13.3	20.1	21.2	<b>14.4</b>	17.0	21.3	31.8	22.0	21.8	20.5	17.7	20.4
C-OccGen [53]	C	23.4	14.5	15.5	9.1	15.3	19.2	7.3	11.3	11.8	8.9	5.9	13.7	34.8	22.0	21.8	19.5	6.0	9.9
L-OccGen† [53]	L	31.6	16.8	18.8	5.1	14.8	19.6	7.0	7.7	11.5	6.7	13.9	14.6	36.4	22.1	22.8	22.3	20.6	24.5
M-OccGen† [53]	C&L	30.3	<b>22.0</b>	24.9	16.4	<b>22.5</b>	26.1	<b>14.0</b>	20.1	21.6	14.6	<b>17.4</b>	<b>21.9</b>	35.8	24.5	24.7	24.0	20.5	23.5
Co-Occ† [39]	C&L	30.6	21.9	26.5	<b>16.8</b>	22.3	<b>27.0</b>	10.1	<b>20.9</b>	20.7	14.5	16.4	21.6	36.9	23.5	25.5	23.7	20.5	23.5
REO (Ours)	C&L	31.7	21.3	<b>24.9</b>	13.1	22.0	25.0	11.5	19.7	<b>22.4</b>	11.1	16.2	21.5	35.2	22.9	24.5	23.9	21.9	25.5
REO †(Ours)	C&L	<b>33.7</b>	21.2	24.4	11.1	20.9	24.6	11.2	16.3	17.5	11.4	16.0	20.8	<b>38.5</b>	<b>25.5</b>	<b>26.0</b>	<b>25.9</b>	<b>22.6</b>	<b>27.1</b>

TABLE 4

3D semantic occupancy prediction results on Occ3D-nuScenes validation set. Cons. Veh represents construction vehicle and Dri. Sur denotes driveable surface, respectively. The **bold** numbers indicate the best results.

Method	mIoU (%)	others	barrier	bicycle	bus	car	Cons. Veh	motorcycle	pedestrian	traffic cone	trailer	truck	Dri. Sur	other flat	sidewalk	terrain	manmade	vegetation
MonoScene [4]	6.06	1.75	7.23	4.26	4.93	9.38	5.67	3.98	3.01	5.90	4.45	7.17	14.91	6.32	7.92	7.43	1.01	7.65
BEVDet [17]	19.38	4.39	30.31	0.23	32.26	34.47	12.97	10.34	10.36	6.26	8.93	23.65	52.27	24.61	26.06	22.31	15.04	15.10
OccFormer [65]	21.93	5.94	30.29	12.32	34.40	39.17	14.44	16.45	17.22	9.27	13.90	26.36	50.99	30.96	34.66	22.73	6.76	6.97
BEVFormer [28]	26.88	5.85	37.83	17.87	40.44	42.43	7.36	23.88	21.81	20.98	22.38	30.70	55.35	28.36	36.00	28.06	20.04	17.69
TPVFormer [18]	27.83	7.22	38.90	13.67	40.78	45.90	17.23	19.99	18.85	14.30	26.69	34.17	55.65	35.47	37.55	30.70	19.40	16.78
CTF-Occ [49]	28.53	8.09	39.33	20.56	38.29	42.24	16.93	24.52	22.72	21.05	22.98	31.11	53.33	33.84	37.98	33.23	20.79	18.00
FB-Occ [29]	42.06	<b>14.30</b>	49.71	<b>30.00</b>	46.62	51.54	29.30	29.13	29.35	30.48	34.97	39.36	83.07	<b>47.16</b>	55.62	59.88	44.89	39.58
PanoOcc [56]	42.13	11.67	50.48	29.64	49.44	55.52	23.29	33.26	30.55	30.99	34.43	42.57	83.31	44.23	54.40	56.04	45.94	40.40
COTR [37]	44.45	13.29	52.11	31.95	46.03	55.63	<b>32.57</b>	32.78	30.35	<b>34.09</b>	37.72	41.84	<b>84.48</b>	46.19	<b>57.55</b>	<b>60.67</b>	51.99	46.33
REO (Ours)	<b>46.51</b>	12.39	<b>55.69</b>	24.10	<b>56.12</b>	<b>57.55</b>	32.20	<b>35.26</b>	<b>40.68</b>	24.95	<b>47.16</b>	<b>49.07</b>	81.45	43.35	52.17	56.87	<b>61.89</b>	<b>59.85</b>

also report the performance of REO with 10-sweeps point clouds, and the number of sampled point cloud voxels is set to 40960. In this case, our REO outperforms the state-of-the-art fusion-based method (*i.e.*, Co-Occ) by 2.8% in geometry IoU.

**Results on Occ3D-nuScenes.** Different from OpenOccupancy, Occ3D-nuScenes is a data set typically for camera-only methods as it considers the visible mask of multi-cameras. We also compare our REO with the advanced camera-centric methods on the Occ3D-nuScenes validation set. As shown in Table 4, our REO achieves the best performance on Occ3D-nuScenes. Specifically, REO outperforms the state-of-the-art method, *i.e.*, COTR [37], by 2.06% in mIoU. Note that the point clouds on nuScenes are collected by a 32-beam LiDAR and are very sparse. As we only fuse 5,120 voxels from point clouds, these results implicit that our REO can effectively reduce the dependency on high-resolution LiDAR.

**Results on SemanticKITTI Scene Completion.** Following [4], [18], we further evaluate our method on SemanticKITTI Scene Completion and compare the performance to existing camera-centric methods, including TPVFormer [18], OccFormer [65], and Symphonies [20]. From Table 5, our REO outperforms existing camera-centric methods by a large margin in both SC IoU and SSC mIoU. Specifically, our REO surpasses the state-of-the-art method (*i.e.*, Symphonies [20]) by 14.64% and 5.65% in SC IoU and SSC mIoU, respectively.

As our REO fuses 20,480 voxels on SemanticKITTI, we investigate the effect of the number of fused point cloud voxels. From table 6, fusing only a few numbers of point cloud voxels

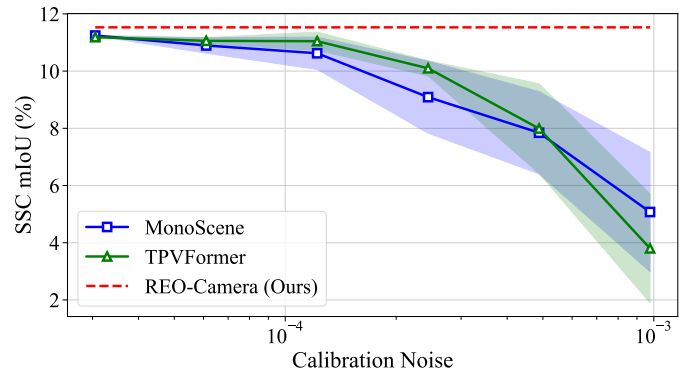


Fig. 6. Comparisons of the model performance under different levels of calibration noise on SemanticKITTI Scene Completion.

brings promising improvement to our REO. Specifically, fusing only 2560 voxels brings 16.61 % and 6.59% improvements in SC IoU and SSC mIoU. Notably, our REO with 2560 point cloud voxels outperforms the state-of-the-art camera-centric method (*i.e.*, Symphonies [20]) by 10.03% and 3.23% in SC IoU and SSC mIoU.

#### 4.4 Efficiency analysis

We analyze the efficiency of our method using a single GeForce RTX 3090 and compare it with existing methods on OpenOccupancy. From Table 7, our REO shows promising efficiency



TABLE 5

Semantic scene completion results on SemanticKITTI validation set. \* represents the RGB-inferred versions of these methods, which are reported in MonoScene [4]. † denotes the reproduced result from TPVFormer [18]. The **bold** numbers indicate the best results.

Method	SC IoU (%)	SSC mIoU (%)	road	sidewalk	parking	other-ground	building	car	truck	bicycle	motorcycle	other-vehicle	vegetation	trunk	terrain	person	bicyclist	motorcyclist	fence	pole	traffic-sign
LMSCNet* [43]	28.61	6.70	40.68	18.22	4.38	0.00	10.31	18.33	0.00	0.00	0.00	0.00	13.66	0.02	20.54	0.00	0.00	0.00	1.21	0.00	0.00
3DSketch* [7]	33.30	7.50	41.32	21.63	0.00	0.00	14.81	18.59	0.00	0.00	0.00	0.00	19.09	0.00	26.40	0.00	0.00	0.00	0.73	0.00	0.00
AICNet* [23]	29.59	8.31	43.55	20.55	11.97	0.07	12.94	14.71	4.53	0.00	0.00	0.00	15.37	2.90	28.71	0.00	0.00	0.00	2.52	0.06	0.00
JS3C-Net* [61]	38.98	10.31	50.49	23.74	11.94	0.07	15.03	24.65	4.41	0.00	0.00	6.15	18.11	4.33	26.86	0.67	0.27	0.00	3.94	3.77	1.45
MonoScene† [4]	36.86	11.08	56.52	26.72	14.27	0.46	14.09	23.26	6.98	0.61	0.45	1.48	17.89	2.81	29.64	1.86	1.20	0.00	5.84	4.14	2.25
TPVFormer [18]	35.61	11.36	56.50	25.87	20.60	0.85	13.88	23.81	8.08	0.36	0.05	4.35	16.92	2.26	30.38	0.51	0.89	0.00	5.94	3.14	1.52
VoxFormer-S [27]	44.02	12.35	54.76	26.35	15.50	0.70	17.65	25.79	5.63	0.59	0.51	3.77	24.39	5.08	29.96	1.78	3.32	0.00	7.64	7.11	4.18
VoxFormer-T [27]	44.15	13.35	53.57	26.52	19.69	0.42	19.54	26.54	7.26	1.28	0.56	7.81	26.10	6.10	33.06	1.93	1.97	0.00	7.31	9.15	4.94
SparseOcc [48]	36.48	13.12	59.59	29.68	20.44	0.47	15.41	24.03	18.07	0.78	0.89	8.94	18.89	3.46	31.06	<b>3.68</b>	0.62	0.00	6.73	3.89	2.60
OccFormer [65]	36.50	13.46	58.85	26.88	19.61	0.31	14.40	25.09	<b>25.53</b>	0.81	1.19	8.52	19.63	3.93	32.62	2.78	2.82	0.00	5.61	4.26	2.86
HASSC-S [54]	44.82	13.48	57.05	28.25	15.90	1.04	19.05	27.23	9.91	0.92	0.86	5.61	25.48	6.15	32.94	2.80	<b>4.71</b>	0.00	6.58	7.68	4.05
H2GFormer-S [58]	44.57	13.73	56.08	29.12	17.83	0.45	19.74	27.60	10.00	0.50	0.47	7.39	26.25	6.80	34.42	1.54	2.88	0.00	7.24	7.88	4.68
H2GFormer-T [58]	44.69	14.29	57.00	29.37	<b>21.74</b>	0.34	20.51	28.21	6.80	0.95	0.91	9.32	27.44	7.80	36.26	1.15	0.10	0.00	7.98	9.88	5.81
HASSC-T [54]	44.58	14.74	57.23	29.08	19.89	<b>1.26</b>	20.19	27.33	17.06	1.07	1.14	8.83	27.01	7.71	33.95	2.25	4.09	0.00	7.95	9.20	4.81
Symphonies [20]	41.92	14.89	56.37	27.58	15.28	0.95	21.64	28.68	20.44	<b>2.54</b>	2.82	13.89	25.72	6.60	30.87	3.52	2.24	0.00	8.40	9.57	5.76
REO (Ours)	<b>56.56</b>	<b>20.54</b>	<b>67.90</b>	<b>37.04</b>	20.13	0.02	<b>32.53</b>	<b>44.04</b>	15.16	0.67	<b>2.86</b>	<b>17.37</b>	<b>39.57</b>	<b>17.51</b>	<b>47.45</b>	2.77	1.18	0.00	<b>13.63</b>	<b>22.14</b>	<b>8.28</b>

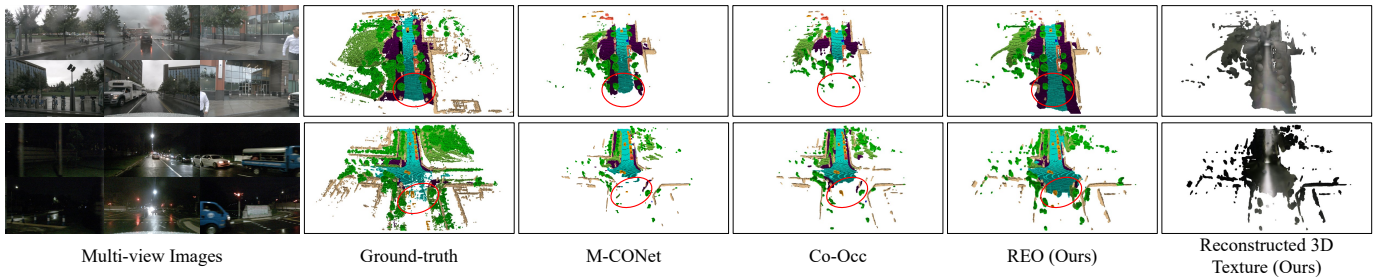


Fig. 7. Qualitative results of REO on OpenOccupancy. We highlight the main differences with red circles. Better viewed by zooming in.

TABLE 6  
Effect of the number of voxels on SemanticKITTI.

#Point cloud voxels	0 (Camera-only)	2560	5120	10240	20480
#Params. (M)↓	39.04	42.70	42.70	42.70	42.70
#FLOPs (G)↓	178	206	216	234	271
SC IoU (%)↑	35.34	51.95	53.42	55.34	<b>56.56</b>
SSC mIoU (%)↑	11.53	18.12	18.85	19.39	<b>20.54</b>

TABLE 7  
Comparisons of model efficiency on OpenOccupancy. † denotes the results with multi-sweep point clouds. The **bold** numbers denote the best results.

Method	#Params.↓	#FLOPs↓	Inference Time↓	mIoU↑	IoU↑
C-CONet [55]	117.99M	2371G	394.77ms	13.6%	21.6%
L-CONet† [55]	65.63M	810G	266.32ms	15.9%	30.1%
M-CONet† [55]	125.34M	3066G	736.50ms	20.5%	26.5%
Co-Occ† [39]	225.68M	–	1460.21ms	<b>21.9%</b>	30.6%
REO (Ours)	<b>43.77M</b>	<b>397G</b>	<b>73.66ms</b>	21.3%	<b>31.7%</b>

compared with existing fusion-based methods. For instance, our REO achieves  $19.8\times$  acceleration compared to Co-Occ [39], with 1.1% improvements in geometry IoU. Moreover, our REO also outperforms M-CONet [55] by 5.2% and 0.8% in geometry IoU and semantic mIoU, respectively, with  $10.0\times$  speedup. These results demonstrate that our method is efficient enough for real-time applications like autonomous driving.

To investigate the efficiency of the proposed calibration-free spatial transformation module, we further report the cost time of spatial transformation w.r.t. single-view image and compare it with the baselines including VoxFormer [27], TPVFormer [18],

TABLE 8  
Detailed inference time of each component in REO. We report the results on SemanticKITTI.

Components	Backbone	Image2BEV	PCD2BEV	Decoder	Total
Cost Time ↓	7.30ms	5.02ms	19.60ms	12.34ms	44.26ms

TABLE 9  
Robustness of REO against calibration noise on SemanticKITTI.

Settings	SC IoU (%)↑	SSC mIoU (%)↑
REO w/o calibration noise	56.56	20.54
REO with calibration noise	56.06	20.43

and MonoScene [4] on SemanticKITTI. As shown in Tables 1 and 8, our CST only takes 11.34% of the total cost time and shows promising efficiency compared to existing methods.

#### 4.5 Robustness against calibration noise

By introducing the calibration-free spatial transformation, our REO can implicitly learn the 2D-to-3D spatial projection from multi-view 2D images. In this way, our method avoids the use of sensor calibration during inference. In contrast, existing methods that rely on sensor calibration may be affected by the calibration noise in practice. To verify this, we apply different levels of Gaussian noise to sensor calibration. Specifically, given the extrinsic of camera  $\mathbf{R} \in \mathbb{R}^{4 \times 4}$ , we adopt the noise by  $\mathbf{R}_{noise} = \mathbf{R} + e$ , where  $e \sim N(\mu, \sigma^2)$ ,  $\mu = 0$  and  $\sigma \in \{2^{-15}, 2^{-14}, 2^{-13}, 2^{-12}, 2^{-11}, 2^{-10}\}$ . As shown in Figure 6, as existing methods rely on sensor calibration, their

TABLE 10

LiDAR segmentation results on nuScenes validation set. Cons. Veh represents construction vehicle and Dri. Sur denotes driveable surface, respectively. The **bold** numbers indicate the best results.

Method	mIoU (%)	barrier	bicycle	bus	car	Cons. Veh	motorcycle	pedestrian	traffic cone	trailer	truck	Dri. Sur	other flat	sidewalk	terrain	manmade	vegetation
BEVFormer [28]	56.2	54.0	22.8	76.7	74.0	45.8	53.1	44.5	24.7	54.7	65.5	88.5	58.1	50.5	52.8	71.0	63.0
OccNet [50]	60.5	67.0	32.6	77.4	73.9	37.6	50.9	51.5	33.7	52.2	67.1	88.7	58.0	58.0	63.1	78.9	77.0
TPVFormer [18]	68.9	70.0	40.9	93.7	85.6	49.8	<b>68.4</b>	59.7	38.2	65.3	83.0	93.3	64.4	64.3	64.5	81.6	79.3
OccFormer [65]	70.4	70.3	43.8	93.2	85.2	52.0	59.1	67.6	45.4	64.4	<b>84.5</b>	93.8	68.2	67.8	68.3	82.1	80.4
PanoOcc [56]	71.6	74.3	43.7	95.4	87.0	<b>56.1</b>	64.6	66.2	41.4	<b>71.5</b>	85.9	95.1	70.1	67.0	68.1	80.9	77.4
REO (Ours)	<b>73.2</b>	<b>75.0</b>	<b>44.5</b>	<b>95.5</b>	<b>92.6</b>	53.6	55.4	<b>69.0</b>	<b>48.9</b>	70.6	84.9	<b>95.4</b>	<b>73.0</b>	<b>71.1</b>	<b>71.9</b>	<b>85.7</b>	<b>83.7</b>

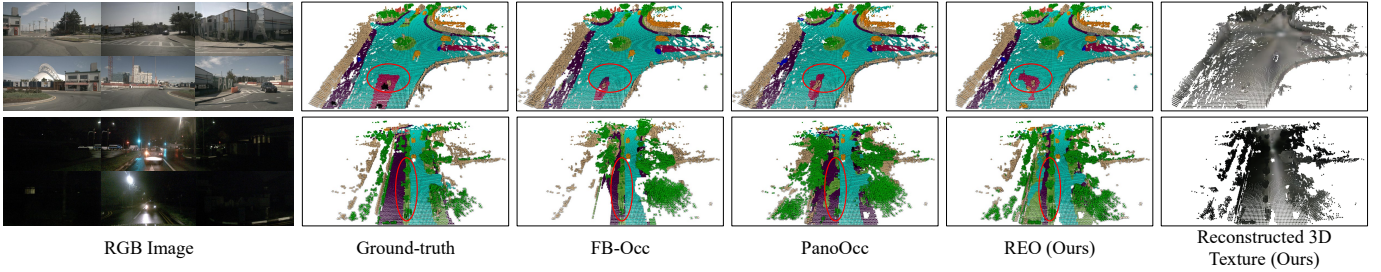


Fig. 8. Qualitative results of REO on Occ3D-nuScenes. We highlight the main differences with red circles. Better viewed by zooming in.

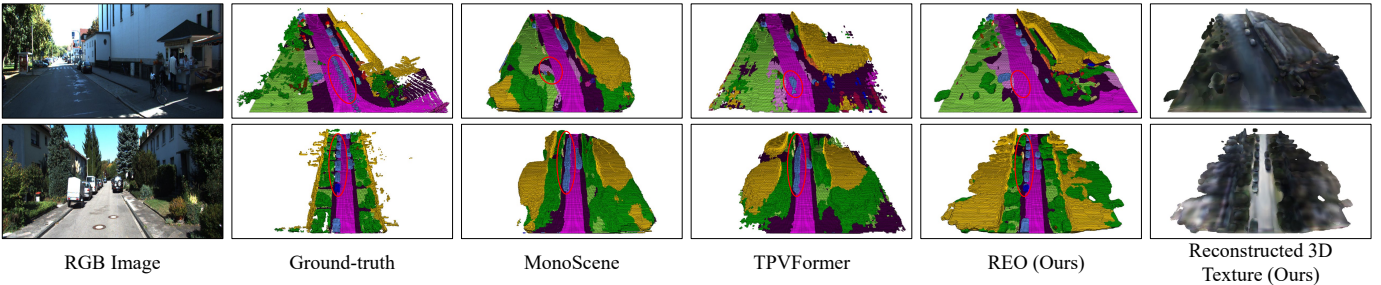


Fig. 9. Qualitative results of REO on SemanticKITTI Scene Completion. We highlight the differences with red circles. Better viewed by zooming in.

model performance is degraded with the increase of calibration noise. In contrast, we do not use the sensor calibration and the spatial projection is learned implicitly with the proposed CST. Therefore, our method is robust to the changes in sensor calibration.

Since our method also uses sensor calibration to build the ground truth of occupancy prediction and 2D/3D auxiliary training tasks, we further investigate the impact of calibration noise during training. Specifically, we apply calibration noise with  $\sigma = 2^{-10}$  ( $\approx 10^{-3}$ ) to the camera extrinsic when constructing ground truth during training. Note that existing methods suffer from significant performance degradation under the same noise level. From Table 9, REO shows promising robustness against calibration noise, as it constructs the 3D space from a larger attention region rather than a single reference point like existing spatial transformation methods.

#### 4.6 Qualitative evaluation

To better understand the benefits of our REO, we visualize the occupancy prediction results on the three benchmarks. Specifically, on OpenOccupancy, we compare our REO with the state-of-the-art fusion-based methods, *i.e.*, M-CONet [55], and Co-Occ [39]. As demonstrated in Figure 7, our REO performs better on

geometry occupancy prediction compared to the baselines. On Occ3D-nuScenes, we compare our REO with FB-Occ [29] and PanoOcc [56]. From Figure 8, all the methods show similar performance at day-time. While at night-time, our REO shows superior performance on semantic occupancy prediction by fusing the spatial information from LiDAR. On SemanticKITTI Scene Completion, we compare our REO with two camera-only baselines, *i.e.*, MonoScene [4], TPVFormer [18]. As demonstrated in Figure 9, our REO shows better scene completion results over the baselines by fusing both information from the camera and LiDAR. Besides, we notice that the ground truth may contain some noise as it is constructed by stacking multi-sweep point clouds. In this case, our REO has better robustness against the noise labels compared to TPVFormer.

#### 4.7 Comparisons on LiDAR semantic segmentation

By replacing the queried voxels with point clouds, our REO can be easily applied to the LiDAR segmentation task. Therefore, we further evaluate the performance of our REO on nuScenes LiDAR segmentation. Following the settings on OpenOccupancy, we use ResNet-50 as the backbone of the 2D image encoder and train the

TABLE 11

Ablation study of the proposed network components on Occ3D-nuScenes validation set. **IFA** denotes image feature aggregation, **BCB** denotes BEV contextual blocks, **Auxiliary Tasks** denotes the proposed 2D/3D auxiliary training tasks. The **bold** numbers denote the best results.

	Baseline	IFA	BCB	Auxiliary Tasks	IoU (%)↑	mIoU (%)↑
1	✓				80.51	42.40
2	✓	✓			80.81	43.04
3	✓	✓	✓		<b>81.97</b>	42.68
4	✓	✓		✓	81.22	46.00
5	✓	✓	✓	✓	81.67	<b>46.22</b>

TABLE 12

Effect of using different stages of image features on Occ3D-nuScenes validation set. The **bold** numbers indicate the best results.

	Stage-1	Stage-2	Stage-3	Stage-4	IoU (%)↑	mIoU (%)↑
1	✓				80.87	39.11
2		✓			<b>81.91</b>	41.69
3			✓		81.74	45.37
4				✓	81.67	<b>46.22</b>
5	✓	✓	✓	✓	81.90	46.21

model for 25 epochs with a batch size of 16. As shown in Table 10, our REO achieves the best performance over the existing occupancy prediction methods, such as OccFormer [65] and PanoOcc [56]. Specifically, our REO outperforms PanoOcc [56] by 1.6% in mIoU.

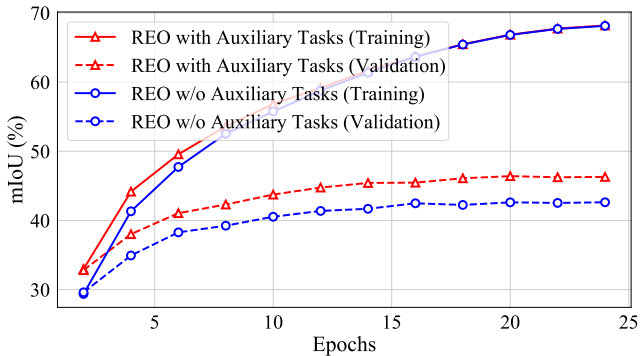


Fig. 10. Training and validation mIoU of REO w/o auxiliary training tasks on Occ3D-nuScenes.

## 5 ABLATION STUDY

### 5.1 Effect of the proposed network components

We study the effect of the proposed network components of REO on Occ3D-nuScenes validation set, including image feature aggregation (IFA), BEV contextual block (BCB), and 2D/3D auxiliary training tasks. Note that we replace the proposed SFA and BCB with a single convolutional layer when investigating the effect of the proposed modules. The hyper-parameters of objectives are empirically set to 1.0. As shown in Table 11, the proposed image feature aggregation brings 0.30% and 0.64% improvements in mIoU and IoU, respectively. By comparing the second and third rows, using BEV contextual block improves the IoU by 1.16%. Moreover, comparing the third and fifth rows, the proposed auxiliary training tasks bring 3.57% mIoU improvement to the occupancy network. In addition, as demonstrated in Figure 10, the proposed auxiliary training tasks effectively help the model learn discriminative features from multi-view images, resulting in better generalization ability on the validation set.

TABLE 13

Effect of  $\lambda_{focal}$ . The **bold** numbers denote the best results.

$\lambda_{focal}$	0	0.5	1.0	1.5	2.0
IoU (%)↑	81.32	81.23	<b>81.67</b>	81.47	81.43
mIoU (%)↑	44.25	45.63	<b>46.22</b>	46.12	45.96

TABLE 14

Effect of  $\lambda_{dice}$ . The **bold** numbers denote the best results.

$\lambda_{dice}$	0	0.5	1.0	1.5	2.0
IoU (%)↑	80.88	81.21	81.67	81.71	<b>81.72</b>
mIoU (%)↑	42.72	<b>46.34</b>	46.22	46.05	45.43

In our spatial-aware feature aggregation module, we fuse the fourth-stage features from the 2D image backbone. As shown in Table 12, we further conduct experiments to investigate the effect of using different stages of features. From the results, using the fourth-stage features from the image backbone achieve the best performance in mIoU. Besides, we also resize the image features to the sample resolution and merge them with a concatenation layer to obtain the performance of using all features. By comparing the fourth and fifth rows, using all stage features only brings marginal improvements in IoU. To trade off the model performance and efficiency, we only use the fourth-stage features from the image backbone in our main experiments.

### 5.2 Effect of hyperparameters in objectives

In this section, we investigate the effect of hyperparameters used in the objectives. First, we set  $\lambda_{dice}, \lambda_{depth}, \lambda_{rgb}$  to 1.0 and train our REO with  $\lambda_{focal} \in \{0, 0.5, 1.0, 1.5, 2.0\}$  on Occ3D-nuScenes. From Table 13, using focal loss significantly improves the semantic classification power of networks. Besides, the model performance is not sensitive to  $\lambda_{focal}$  when increasing  $\lambda_{focal}$  from 0.5 to 2.0. Second, we set  $\lambda_{focal}, \lambda_{depth}, \lambda_{rgb}$  to 1.0 and train the model with  $\lambda_{dice} \in \{0, 0.5, 1.0, 1.5, 2.0\}$ . As shown in Table 14, using dice loss can effectively improve the model performance in both geometry IoU and semantic mIoU. However, with the increasing of  $\lambda_{dice}$ , performance in semantic mIoU is degraded while the performance in geometry occupancy prediction is slightly improved. To trade off geometry and semantic occupancy prediction performance, we use  $\lambda_{dice} = 1$  in our main experiments. Third, we set  $\lambda_{focal}, \lambda_{dice}, \lambda_{rgb}$  to 1 and train the model with  $\lambda_{depth} \in \{0, 1.0, 2.0, 4.0, 8.0\}$ . From Table 15, the model performance in semantic occupancy prediction can be improved by introducing a depth regression task. We then use  $\lambda_{depth} = 2.0$  and train model with  $\lambda_{rgb} \in \{0, 1.0, 2.0, 4.0, 8.0\}$  to study the effect of the texture reconstruction task. As shown in Table 16, using texture reconstruction can further improve the model performance in mIoU.

### 5.3 Effect of using different image backbones

We investigate the effect of using different image backbones, *i.e.*, ResNet-18, ResNet-34, ResNet-50, ResNet-101, and ResNet-152 on Occ3D-nuScenes validation set. As shown in Table 17, using deeper networks can bring performance gains to our method. For example, using ResNet-50 as backbones outperforms the model with ResNet-34 by 0.36% and 1.79% in geometry IoU and semantic mIoU, respectively. Note that deeper networks also require more computation resources. Therefore, we use ResNet-50 as the backbone to extract the image features from multi-cameras.



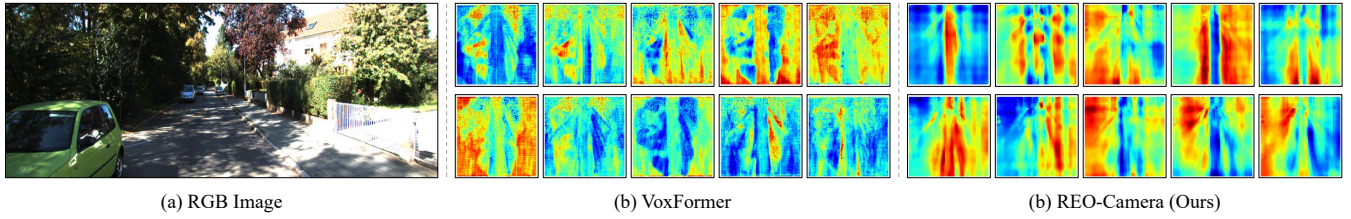


Fig. 11. Visualization results of the projected BEV features. For clarity, we only show the first 10 BEV features of both VoxFormer and REO on SemanticKITTI. Better viewed by zooming in.

TABLE 15  
Effect of  $\lambda_{depth}$ . The **bold** numbers denote the best results.

$\lambda_{depth}$	0	1.0	2.0	4.0	8.0
IoU (%) $\uparrow$	81.88	81.67	81.91	81.70	<b>82.11</b>
mIoU (%) $\uparrow$	45.94	46.22	<b>46.51</b>	46.30	46.11

TABLE 16  
Effect of  $\lambda_{rgb}$ . The **bold** number denotes the best result.

$\lambda_{rgb}$	0	1.0	2.0	4.0	8.0
IoU (%) $\uparrow$	81.70	<b>81.91</b>	81.72	81.15	81.44
mIoU (%) $\uparrow$	45.85	46.51	46.57	46.60	<b>46.86</b>

#### 5.4 Effect of different resolutions of image

We further study the effect of using different resolutions of RGB images as inputs. Specifically, we train the models with resolutions of  $224 \times 416$ ,  $448 \times 800$ , and  $896 \times 1600$ , and report the results on Occ3D-nuScenes validation set. As shown in Table 18, using a higher resolution of input images can further improve the model performance. However, it also leads to higher computational complexity of the model. For instance, the model with a resolution of  $896 \times 1600$  requires  $3.0\times$  of computational costs more than the one with a resolution of  $448 \times 800$ .

#### 5.5 Visualization of the projected BEV features

To investigate the 2D-to-3D spatial projection learned by our calibration-free spatial transformation, we visualize the BEV feature maps of our REO on SemanticKITTI and compare the results to VoxFormer [27] for better illustration. For fair comparisons, we visualize the features from REO-Camera that use RGB images as inputs only. As shown in Figure 11, our REO shows similar feature patterns as VoxFormer. These results prove that our CST can learn spatial correspondence even without using calibration information as inputs. Besides, we also observe that the features learned by our CST have better spatial continuity compared to those of VoxFormer, as our CST uses vanilla cross attention to model the spatial correspondence globally.

## 6 CONCLUSION

In this work, we proposed the calibration-free spatial transformation for robust and efficient semantic occupancy prediction. Different from the existing methods that explicitly use sensor calibration information to project the 2D RGB images to 3D space, we exploited a calibration-free projection method based on the vanilla cross-attention scheme and introduced a set of 2D/3D auxiliary training tasks to enhance the discrimination power of image backbones on both spatial and semantic features. Besides, our

TABLE 17  
Effect of using different image backbones on Occ3D-nuScenes validation set. The **bold** numbers indicate the best results.

Backbones	R-18	R-34	R-50	R-101	R-152
#Params. (M) $\downarrow$	28.28	38.39	41.21	60.20	75.84
#FLOPs (G) $\downarrow$	186	265	285	444	604
IoU (%) $\uparrow$	81.55	81.78	<b>81.91</b>	81.61	81.55
mIoU (%) $\uparrow$	44.72	45.87	46.51	46.59	<b>46.72</b>

TABLE 18  
Effect of different resolutions of the image. The **bold** numbers indicate the best results

Resolution	#Params.(M) $\downarrow$	#FLOPs(G) $\downarrow$	IoU (%) $\uparrow$	mIoU (%) $\uparrow$
$224 \times 416$	40.51	144	81.72	43.60
$448 \times 800$	41.21	285	81.91	46.51
$896 \times 1600$	44.03	863	<b>82.25</b>	<b>47.60</b>

method is flexible to fuse different modalities to achieve better performance. The experimental results on three benchmarks showed the superiority of our method on both the robustness against calibration-noise and model efficiency for real-time application. In the future, we will fuse more modalities, including Radar and infrared cameras to further improve the model performance. In addition, we will try to apply our method to more perception tasks, such as road structure perception.

## REFERENCES

- [1] J. Behley, M. Garbade, A. Milioto, J. Quenzel, S. Behnke, C. Stachniss, and J. Gall. SemanticKITTI: A dataset for semantic scene understanding of lidar sequences. In *IEEE International Conference on Computer Vision*, pages 9297–9307, 2019.
- [2] A. Bochkovskiy, C.-Y. Wang, and H.-Y. M. Liao. Yolov4: Optimal speed and accuracy of object detection. *arXiv preprint arXiv:2004.10934*, pages 1–17, 2020.
- [3] H. Caesar, V. Bankiti, A. H. Lang, S. Vora, V. E. Liong, Q. Xu, A. Krishnan, Y. Pan, G. Baldan, and O. Beijbom. nuscenes: A multimodal dataset for autonomous driving. In *IEEE Conference on Computer Vision and Pattern Recognition*, pages 11621–11631, 2020.
- [4] A.-Q. Cao and R. de Charette. Monoscene: Monocular 3d semantic scene completion. In *IEEE Conference on Computer Vision and Pattern Recognition*, pages 3991–4001, 2022.
- [5] P. Chen, D. Ji, K. Lin, W. Hu, W. Huang, T. Li, M. Tan, and C. Gan. Learning active camera for multi-object navigation. *Advances in Neural Information Processing Systems*, 35:28670–28682, 2022.
- [6] S. Chen, T. Cheng, X. Wang, W. Meng, Q. Zhang, and W. Liu. Efficient and robust 2d-to-bev representation learning via geometry-guided kernel transformer. *arXiv preprint arXiv:2206.04584*, pages 1–5, 2022.
- [7] X. Chen, K.-Y. Lin, C. Qian, G. Zeng, and H. Li. 3d sketch-aware semantic scene completion via semi-supervised structure prior. In *IEEE Conference on Computer Vision and Pattern Recognition*, pages 4193–4202, 2020.
- [8] X. Chen, T. Zhang, Y. Wang, Y. Wang, and H. Zhao. Futr3d: A unified sensor fusion framework for 3d detection. In *IEEE Conference on Computer Vision and Pattern Recognition*, pages 172–181, 2023.

- [9] T. Cortinhal, G. Tzelepis, and E. Erdal Aksoy. Salsanext: Fast, uncertainty-aware semantic segmentation of lidar point clouds. In *International Symposium on Visual Computing*, pages 207–222. Springer, 2020.
- [10] K. El Madawi, H. Rashed, A. El Sallab, O. Nasr, H. Kamel, and S. Yogamani. Rgb and lidar fusion based 3d semantic segmentation for autonomous driving. In *IEEE Intelligent Transportation Systems Conference*, pages 7–12. IEEE, 2019.
- [11] A. Geiger, P. Lenz, and R. Urtasun. Are we ready for autonomous driving? the kitti vision benchmark suite. In *IEEE Conference on Computer Vision and Pattern Recognition*, pages 3354–3361. IEEE, 2012.
- [12] B. Graham, M. Engelcke, and L. Van Der Maaten. 3d semantic segmentation with submanifold sparse convolutional networks. In *IEEE Conference on Computer Vision and Pattern Recognition*, pages 9224–9232, 2018.
- [13] J. Gu, C. Hu, T. Zhang, X. Chen, Y. Wang, Y. Wang, and H. Zhao. Vip3d: End-to-end visual trajectory prediction via 3d agent queries. In *IEEE Conference on Computer Vision and Pattern Recognition*, pages 5496–5506, 2023.
- [14] K. He, X. Chen, S. Xie, Y. Li, P. Dollár, and R. Girshick. Masked autoencoders are scalable vision learners. In *IEEE Conference on Computer Vision and Pattern Recognition*, pages 16000–16009, 2022.
- [15] K. He, X. Zhang, S. Ren, and J. Sun. Deep residual learning for image recognition. In *IEEE Conference on Computer Vision and Pattern Recognition*, pages 770–778, 2016.
- [16] Y. Hu, J. Yang, L. Chen, K. Li, C. Sima, X. Zhu, S. Chai, S. Du, T. Lin, W. Wang, et al. Planning-oriented autonomous driving. In *IEEE Conference on Computer Vision and Pattern Recognition*, pages 17853–17862, 2023.
- [17] J. Huang, G. Huang, Z. Zhu, Y. Ye, and D. Du. Bevdet: High-performance multi-camera 3d object detection in bird-eye-view. *arXiv preprint arXiv:2112.11790*, pages 1–19, 2021.
- [18] Y. Huang, W. Zheng, Y. Zhang, J. Zhou, and J. Lu. Tri-perspective view for vision-based 3d semantic occupancy prediction. In *IEEE Conference on Computer Vision and Pattern Recognition*, pages 9223–9232, 2023.
- [19] M. Jaritz, T.-H. Vu, R. d. Charette, E. Wirbel, and P. Pérez. xmuda: Cross-modal unsupervised domain adaptation for 3d semantic segmentation. In *IEEE Conference on Computer Vision and Pattern Recognition*, pages 12605–12614, 2020.
- [20] H. Jiang, T. Cheng, N. Gao, H. Zhang, T. Lin, W. Liu, and X. Wang. Symphonize 3d semantic scene completion with contextual instance queries. In *IEEE Conference on Computer Vision and Pattern Recognition*, pages 20258–20267, 2024.
- [21] H. Jiang, W. Meng, H. Zhu, Q. Zhang, and J. Yin. Multi-camera calibration free bev representation for 3d object detection. *arXiv preprint arXiv:2210.17252*, pages 1–15, 2022.
- [22] J. Krantz, E. Wijnmans, A. Majumdar, D. Batra, and S. Lee. Beyond the nav-graph: Vision-and-language navigation in continuous environments. In *European Conference on Computer Vision*, pages 104–120. Springer, 2020.
- [23] J. Li, K. Han, P. Wang, Y. Liu, and X. Yuan. Anisotropic convolutional networks for 3d semantic scene completion. In *IEEE Conference on Computer Vision and Pattern Recognition*, pages 3351–3359, 2020.
- [24] Y. Li, H. Bao, Z. Ge, J. Yang, J. Sun, and Z. Li. Bevestereo: Enhancing depth estimation in multi-view 3d object detection with temporal stereo. In *AAAI Conference on Artificial Intelligence*, volume 37, pages 1486–1494, 2023.
- [25] Y. Li, Z. Ge, G. Yu, J. Yang, Z. Wang, Y. Shi, J. Sun, and Z. Li. Bevdepth: Acquisition of reliable depth for multi-view 3d object detection. In *AAAI Conference on Artificial Intelligence*, volume 37, pages 1477–1485, 2023.
- [26] Y. Li, A. W. Yu, T. Meng, B. Caine, J. Ngiam, D. Peng, J. Shen, Y. Lu, D. Zhou, Q. V. Le, et al. Deepfusion: Lidar-camera deep fusion for multi-modal 3d object detection. In *IEEE Conference on Computer Vision and Pattern Recognition*, pages 17182–17191, 2022.
- [27] Y. Li, Z. Yu, C. Choy, C. Xiao, J. M. Alvarez, S. Fidler, C. Feng, and A. Anandkumar. Voxformer: Sparse voxel transformer for camera-based 3d semantic scene completion. In *IEEE Conference on Computer Vision and Pattern Recognition*, pages 9087–9098, 2023.
- [28] Z. Li, W. Wang, H. Li, E. Xie, C. Sima, T. Lu, Y. Qiao, and J. Dai. Bevformer: Learning bird’s-eye-view representation from multi-camera images via spatiotemporal transformers. In *European Conference on Computer Vision*, pages 1–18. Springer, 2022.
- [29] Z. Li, Z. Yu, W. Wang, A. Anandkumar, T. Lu, and J. M. Alvarez. Fb-bev: Bev representation from forward-backward view transformations. In *IEEE International Conference on Computer Vision*, pages 6919–6928, 2023.
- [30] Y. Liao, J. Xie, and A. Geiger. Kitti-360: A novel dataset and benchmarks for urban scene understanding in 2d and 3d. *IEEE Transactions on Pattern Analysis and Machine Intelligence*, 45(3):3292–3310, 2022.
- [31] T.-Y. Lin, P. Goyal, R. Girshick, K. He, and P. Dollár. Focal loss for dense object detection. In *IEEE International Conference on Computer Vision*, pages 2980–2988, 2017.
- [32] Y. Liu, R. Chen, X. Li, L. Kong, Y. Yang, Z. Xia, Y. Bai, X. Zhu, Y. Ma, Y. Li, et al. Uniseg: A unified multi-modal lidar segmentation network and the openpcseg codebase. In *IEEE International Conference on Computer Vision*, pages 21662–21673, 2023.
- [33] Y. Liu, T. Wang, X. Zhang, and J. Sun. Petr: Position embedding transformation for multi-view 3d object detection. In *European Conference on Computer Vision*, pages 531–548. Springer, 2022.
- [34] I. Loshchilov and F. Hutter. Sgdr: Stochastic gradient descent with warm restarts. In *International Conference on Learning Representations*, pages 1–16, 2017.
- [35] I. Loshchilov and F. Hutter. Decoupled weight decay regularization. In *International Conference on Learning Representations*, pages 1–19, 2019.
- [36] C. Lu, F. Yin, X. Chen, W. Liu, T. Chen, G. Yu, and J. Fan. A large-scale outdoor multi-modal dataset and benchmark for novel view synthesis and implicit scene reconstruction. In *IEEE International Conference on Computer Vision*, pages 7557–7567, 2023.
- [37] Q. Ma, X. Tan, Y. Qu, L. Ma, Z. Zhang, and Y. Xie. Cotr: Compact occupancy transformer for vision-based 3d occupancy prediction. In *IEEE Conference on Computer Vision and Pattern Recognition*, pages 19936–19945, 2024.
- [38] G. P. Meyer, J. Charland, D. Hegde, A. Laddha, and C. Vallespi-Gonzalez. Sensor fusion for joint 3d object detection and semantic segmentation. In *IEEE Conference on Computer Vision and Pattern Recognition Workshops*, pages 1–8, 2019.
- [39] J. Pan, Z. Wang, and L. Wang. Co-occ: Coupling explicit feature fusion with volume rendering regularization for multi-modal 3d semantic occupancy prediction. *IEEE Robotics and Automation Letters*, pages 5687–5694, 2024.
- [40] A. Paszke, S. Gross, F. Massa, A. Lerer, J. Bradbury, G. Chanan, T. Killeen, Z. Lin, N. Gimelshein, L. Antiga, et al. Pytorch: An imperative style, high-performance deep learning library. In *Advances in Neural Information Processing Systems*, pages 8026–8037, 2019.
- [41] J. Philion and S. Fidler. Lift, splat, shoot: Encoding images from arbitrary camera rigs by implicitly unprojecting to 3d. In *European Conference on Computer Vision*, pages 194–210. Springer, 2020.
- [42] T. Roddick, A. Kendall, and R. Cipolla. Orthographic feature transform for monocular 3d object detection. *arXiv preprint arXiv:1811.08188*, pages 1–10, 2018.
- [43] L. Roldao, R. de Charette, and A. Verroust-Blondet. Lmscnet: Lightweight multiscale 3d semantic completion. In *International Conference on 3D Vision*, pages 111–119. IEEE, 2020.
- [44] D. Rukhovich, A. Vorontsova, and A. Konushin. Imvoxelnet: Image to voxels projection for monocular and multi-view general-purpose 3d object detection. In *Winter Conference on Applications of Computer Vision*, pages 2397–2406, 2022.
- [45] C. H. Sudre, W. Li, T. Vercauteren, S. Ourselin, and M. Jorge Cardoso. Generalised dice overlap as a deep learning loss function for highly unbalanced segmentations. In *Deep Learning in Medical Image Analysis and Multimodal Learning for Clinical Decision Support*, pages 240–248. Springer, 2017.
- [46] P. Sun, H. Kretzschmar, X. Dotiwalla, A. Chouard, V. Patnaik, P. Tsui, J. Guo, Y. Zhou, Y. Chai, B. Caine, et al. Scalability in perception for autonomous driving: Waymo open dataset. In *IEEE Conference on Computer Vision and Pattern Recognition*, pages 2446–2454, 2020.
- [47] M. Tan, Z. Zhuang, S. Chen, R. Li, K. Jia, Q. Wang, and Y. Li. Epmf: Efficient perception-aware multi-sensor fusion for 3d semantic segmentation. *IEEE Transactions on Pattern Analysis and Machine Intelligence*, pages 1–15, 2024.
- [48] P. Tang, Z. Wang, G. Wang, J. Zheng, X. Ren, B. Feng, and C. Ma. Sparseocc: Rethinking sparse latent representation for vision-based semantic occupancy prediction. In *IEEE Conference on Computer Vision and Pattern Recognition*, pages 15035–15044, 2024.
- [49] X. Tian, T. Jiang, L. Yun, Y. Mao, H. Yang, Y. Wang, Y. Wang, and H. Zhao. Occ3d: A large-scale 3d occupancy prediction benchmark for autonomous driving. *Advances in Neural Information Processing Systems*, 36:64318–64330, 2024.
- [50] W. Tong, C. Sima, T. Wang, L. Chen, S. Wu, H. Deng, Y. Gu, L. Lu, P. Luo, D. Lin, et al. Scene as occupancy. In *IEEE International Conference on Computer Vision*, pages 8406–8415, 2023.
- [51] A. Vaswani, N. Shazeer, N. Parmar, J. Uszkoreit, L. Jones, A. N. Gomez, Ł. Kaiser, and I. Polosukhin. Attention is all you need. *Advances in Neural Information Processing Systems*, 30, 2017.

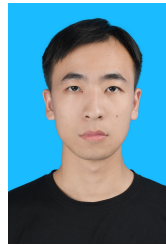
- [52] S. Vora, A. H. Lang, B. Helou, and O. Beijbom. Pointpainting: Sequential fusion for 3d object detection. In *IEEE Conference on Computer Vision and Pattern Recognition*, pages 4604–4612, 2020.
- [53] G. Wang, Z. Wang, P. Tang, J. Zheng, X. Ren, B. Feng, and C. Ma. Occgen: Generative multi-modal 3d occupancy prediction for autonomous driving. *arXiv preprint arXiv:2404.15014*, pages 1–31, 2024.
- [54] S. Wang, J. Yu, W. Li, W. Liu, X. Liu, J. Chen, and J. Zhu. Not all voxels are equal: Hardness-aware semantic scene completion with self-distillation. In *IEEE Conference on Computer Vision and Pattern Recognition*, pages 14792–14801, 2024.
- [55] X. Wang, Z. Zhu, W. Xu, Y. Zhang, Y. Wei, X. Chi, Y. Ye, D. Du, J. Lu, and X. Wang. Openoccupancy: A large scale benchmark for surrounding semantic occupancy perception. In *IEEE International Conference on Computer Vision*, pages 17850–17859, October 2023.
- [56] Y. Wang, Y. Chen, X. Liao, L. Fan, and Z. Zhang. Panoocc: Unified occupancy representation for camera-based 3d panoptic segmentation. In *IEEE Conference on Computer Vision and Pattern Recognition*, pages 17158–17168, 2024.
- [57] Y. Wang, V. C. Guizilini, T. Zhang, Y. Wang, H. Zhao, and J. Solomon. Detr3d: 3d object detection from multi-view images via 3d-to-2d queries. In *Conference on Robot Learning*, pages 180–191. PMLR, 2022.
- [58] Y. Wang and C. Tong. H2gformer: Horizontal-to-global voxel transformer for 3d semantic scene completion. In *AAAI Conference on Artificial Intelligence*, volume 38, pages 5722–5730, 2024.
- [59] Y. Wei, L. Zhao, W. Zheng, Z. Zhu, J. Zhou, and J. Lu. Surroundocc: Multi-camera 3d occupancy prediction for autonomous driving. In *IEEE International Conference on Computer Vision*, pages 21729–21740, 2023.
- [60] H. Xu, J. Chen, S. Meng, Y. Wang, and L.-P. Chau. A survey on occupancy perception for autonomous driving: The information fusion perspective. *Information Fusion*, 114:102671, 2025.
- [61] X. Yan, J. Gao, J. Li, R. Zhang, Z. Li, R. Huang, and S. Cui. Sparse single sweep lidar point cloud segmentation via learning contextual shape priors from scene completion. In *AAAI Conference on Artificial Intelligence*, volume 35, pages 3101–3109, 2021.
- [62] X. Yan, J. Gao, C. Zheng, C. Zheng, R. Zhang, S. Cui, and Z. Li. 2dpass: 2d priors assisted semantic segmentation on lidar point clouds. In *European Conference on Computer Vision*, pages 677–695. Springer, 2022.
- [63] B. Yang, W. Luo, and R. Urtasun. Pixor: Real-time 3d object detection from point clouds. In *IEEE Conference on Computer Vision and Pattern Recognition*, pages 7652–7660, 2018.
- [64] T. Yin, X. Zhou, and P. Krahenbuhl. Center-based 3d object detection and tracking. In *IEEE Conference on Computer Vision and Pattern Recognition*, pages 11784–11793, 2021.
- [65] Y. Zhang, Z. Zhu, and D. Du. Occformer: Dual-path transformer for vision-based 3d semantic occupancy prediction. In *IEEE International Conference on Computer Vision*, pages 9433–9443, 2023.
- [66] Z. Zhang, Z. Zhang, Q. Yu, R. Yi, Y. Xie, and L. Ma. Lidar-camera panoptic segmentation via geometry-consistent and semantic-aware alignment. In *IEEE International Conference on Computer Vision*, pages 3662–3671, 2023.
- [67] B. Zhou and P. Krähenbühl. Cross-view transformers for real-time map-view semantic segmentation. In *IEEE Conference on Computer Vision and Pattern Recognition*, pages 13760–13769, 2022.
- [68] H. Zhou, Z. Ge, Z. Li, and X. Zhang. Matrixvt: Efficient multi-camera to bev transformation for 3d perception. In *IEEE Conference on Computer Vision and Pattern Recognition*, pages 8548–8557, 2023.
- [69] Z. Zhou, Y. Zhang, and H. Foroosh. Panoptic-polarnet: Proposal-free lidar point cloud panoptic segmentation. In *IEEE Conference on Computer Vision and Pattern Recognition*, pages 13194–13203, 2021.
- [70] Z. Zhuang, R. Li, K. Jia, Q. Wang, Y. Li, and M. Tan. Perception-aware multi-sensor fusion for 3d lidar semantic segmentation. In *IEEE International Conference on Computer Vision*, pages 16280–16290, 2021.
- [71] S. Zuo, W. Zheng, Y. Huang, J. Zhou, and J. Lu. Pointocc: Cylindrical tri-perspective view for point-based 3d semantic occupancy prediction. *arXiv preprint arXiv:2308.16896*, pages 1–12, 2023.



**Zhuangwei Zhuang** is a Ph.D. student in the School of Software Engineering at South China University of Technology, and is currently working as an intern at RoboSense Inc., Shenzhen, China. He received his Bachelor Degree in Automation and Engineering in 2016 and Master Degree in Software Engineering in 2018, both from South China University of Technology in Guangzhou, China. His research interests include model compression and 3D scene understanding for autonomous driving.



**Ziyin Wang** is currently working as an AI director at RoboSense Inc., Shenzhen, China. He received the Bachelor Degree in 2013 at the School of Electrical Engineering from the East China University of Science and Technology, Shanghai, China. In 2019, he received the Ph.D. degree at the Department of Computer Science, Purdue University, West Lafayette, IN, USA. His research interests include autonomous driving, machine learning, and image understanding.



**Sitao Chen** is a Master student in the School of Software Engineering at South China University of Technology. He received his Bachelor Degree in the School of Mechanical & Automotive in 2023 from South China University of Technology in Guangzhou, China. His research interests include 3D scene understanding for autonomous driving.



**Lizhao Liu** is a Master student in the School of Software Engineering at South China University of Technology. He received his Bachelor Degree in the School of Software Engineering in 2021 from South China University of Technology in Guangzhou, China. His main research interests cover visual recognition and multimodal learning.



**Hui Luo** is currently pursuing a Ph.D. in signal and information processing at the University of Chinese Academy of Sciences in Beijing, China. During his Ph.D. program, he also conducts research at the Institute of Optics and Electronics, Chinese Academy of Sciences, located in Chengdu, China. His research interests include model compression and acceleration, as well as developing robust and reliable models.



**Mingkui Tan** is currently a Professor at the School of Software Engineering, South China University of Technology, Guangzhou, China. He received the Bachelor Degree in Environmental Science and Engineering in 2006 and the Master Degree in Control Science and Engineering in 2009, both from Hunan University in Changsha, China. He received the Ph.D. degree in Computer Science from Nanyang Technological University, Singapore, in 2014. From 2014-2016, he worked as a Senior Research Associate on computer vision at the School of Computer Science, University of Adelaide, Australia. His research interests include machine learning, sparse analysis, deep learning, and large-scale optimization.